Optics Letters

Continuous variable spin–orbit total angular momentum entanglement on the higher-order Poincaré sphere

Hui Guo, Na Liu, Hengxin Sun, Kui Liu,* and Jiangrui Gao

State Key Laboratory of Quantum Optics and Quantum Optics Devices, Institute of Opto-Electronics, Collaborative Innovation Center of Extreme Optics, Shanxi University, Taiyuan 030006, China
*Corresponding author: liukui@sxu.edu.cn

Received 13 February 2023; accepted 24 February 2023; posted 27 February 2023; published 23 March 2023

Optical spin–orbit coupling is an important phenomenon and has fruitful applications. Here, we investigate the spin–orbit total angular momentum entanglement in the optical parametric downconversion process. Four pairs of entangled vector vortex modes are experimentally generated directly using a dispersion- and astigmatism-compensated single optical parametric oscillator, and for the first time, to the best of our knowledge, the spin–orbit quantum states are characterized on the quantum higher-order Poincaré sphere, and the relationship of spin–orbit total angular momentum Stokes entanglement is demonstrated. These states have potential applications in high-dimensional quantum communication and multiparameter measurement.

https://doi.org/10.1364/OL.487569

The spin angular momentum (SAM) and orbital angular momentum (OAM) of light are associated with the polarization and the phase distribution of the light state, respectively. Vector vortex (VV) fields involved in the coupling of SAM and OAM [1] are an important field of research [2]. The fields have found many applications in laser materials processing [3], optical metrology [4], as well as in fundamental quantum mechanics [5] and quantum information science [6,7], especially in space-based [8] or fiber-based [9,10] quantum communication.

Squeezed and entangled optical fields are essential resources in the continuous variable (CV) quantum optics and quantum information communities. The CV quantum SAM states are the first generated [11] and characterized by CV quantum Stokes parameters on a Poincaré sphere [12,13]. Such a graphical representation has also been extensively investigated on the OAM Stokes operator [14]. Then, direct experimental characterization of CV quantum OAM Stokes-operator squeezing [15] and the OAM Stokes-operator entanglement [16] are also reported. Moreover, a CV hyperentanglement of SAM and OAM is demonstrated in the optical parametric downconversion process [17]. Generation and accurate characterization of the SAM and OAM quantum states are necessary for these states to fulfill their potential in the field of quantum information [18]. These will allow direct experimental observation of the commutation relations in the CV regime, provide a useful tool for studying the interaction between light and media, and serve as additional channels in high-capacity quantum communication. Thus, the spin–orbit quantum states are more attractive due to them containing the full angular momentum of the OAM and SAM. Such states, involving spin–orbit coupling, may have more widespread applications in quantum information processing and material characterizations. However, the progress in generating CV entanglement between VV modes remains in its infancy. The CV squeezed first-order VV mode was experimentally realized by exploiting the nonlinear Kerr effect in a fiber [19], and the squeezed high-order VV modes were also generated [20]. Barros *et al.* also theoretically pointed out the possible hybrid-entanglement between spin and orbit Stokes parameters. The direct experimental generation of CV nonclassical VV modes in the optical parametric oscillator (OPO) process hindered by astigmatism and dispersion [21], especially the CV quantum properties research of the spin–orbit total angular momentum Stokes parameters, has not, to our knowledge, been presented.

Here, we generate the continuous variable spin–orbit modes entanglement using a type-II OPO, and characterize the higher-order Poincaré sphere (HOPS) Stokes parameters entanglement. First, the spin–orbit coupling in the optical parametric downconversion process is investigated. By compensating the dispersion and astigmatism of the OPO, four pairs of spin–orbit modes entanglement are simultaneously generated and verified by measuring quadrature entanglement between first-order HG modes. In addition, the entanglement of an arbitrary pair of VV modes on HOPS is demonstrated. Finally, we expand Stokes entanglement to the higher-order Poincaré sphere and give a characterization of the CV spin–orbit total angular momentum Stokes entanglement. Unlike the case of SAM or OAM Stokes entanglement [12,15], the conditional quantum uncertainty volume of the OPO output becomes a small spheroid. These quantum correlations can be useful to study the quantum spin–orbit coupling interaction in various scenarios.

SAM and OAM have been extensively explored and characterized in terms of the quantum Stokes operators. Likewise, we define the Stokes operator analogs for the VV modes according

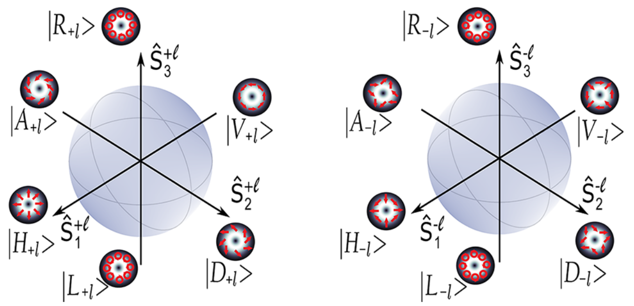

Fig. 1. Higher-order Poincaré sphere of the first-order VV modes. Points on the sphere are associated with a superposition of SAM and OAM. The optical vortex and circular polarization handedness of each pole are the same (the sphere on the right, $\hat{S}^{-l}$) or opposite (the sphere on the left, $\hat{S}^{+l}$). The modes on the $\hat{S}_1^{\pm l}$ region are well-known fiber modes.

to their classical representation on HOPS [22] as

$$\begin{aligned} \hat{S}_1^l &= \hat{a}_{H_l}^+\hat{a}_{H_l} - \hat{a}_{V_l}^+\hat{a}_{V_l}, \\ \hat{S}_2^l &= \hat{a}_{D_l}^+\hat{a}_{D_l} - \hat{a}_{A_l}^+\hat{a}_{A_l}, \\ \hat{S}_3^l &= \hat{a}_{R_l}^+\hat{a}_{R_l} - \hat{a}_{L_l}^+\hat{a}_{L_l}, \end{aligned} \tag{1}$$

where $\hat{a}^+$ and $\hat{a}$ are the creation and annihilation operators for the various first-order VV modes. The topological charge magnitude $|l|$ ($l = \pm1, \pm2, \pm3, \ldots$) define the "order" of the VV modes. As Eq. (1) shows, $\hat{S}_1^l$, $\hat{S}_2^l$, and $\hat{S}_3^l$ represent the difference in the photon numbers between the two VV modes, LG_0^l mode with horizontal and vertical polarization (H_l and V_l), LG_0^l mode with diagonal and antidiagonal polarization (D_l and A_l), and LG_0^l mode with right circular polarization and left circular polarization (R_l and L_l), respectively. These operators follow the same algebra as the Stokes operators. The commutation relations are $[\hat{S}_p^l, \hat{S}_q^{l'}] = 2i\delta_{ll'}\hat{S}_k^l$, where $p, q, k \in \{1, 2, 3\}$ of cyclic permutation and $l, l' \in \{-1, +1, -2, +2, \ldots\}$.

As depicted in Fig. 1, the first-order VV modes are described by two spheres. The HOPS for $l = 1$ characterize a VV mode with total optical angular momentum per photon of zero, which enables the VV modes propagation invariant under arbitrary rotations about the z axis. This unique feature is valuable for alignment-free communication in space-based quantum networks. The other HOPS for $l = -1$ describe a VV mode with total optical angular momentum per photon of $2\hbar$. It may find application in rotation-sensitive quantum measurements [23].

In the type-II optical parametric downconversion process, the OPO is capable to output high-dimensional entanglement with three degrees of freedom (frequency, SAM, and OAM). Under spin–orbit coupling, the output fields of VV modes are formed. Among them, the downconverted photon pair, A and B, have orthogonal polarization and satisfy the conservation of angular momentum ($\hat{a}_{H_{\pm l}}$and$\hat{b}_{V_{\mp l}}$), and obey the conservation of energy ($\hat{a}_{\pm n\Omega}$and$\hat{b}_{\mp n\Omega}$). Here, Ω is the free spectrum range (FSR) of the OPO and n is the order of the frequency sideband.

Hence, the corresponding Hamiltonian of the first-order frequency sideband in the system is expressed by

$$\begin{aligned} \hat{H}_{int} = i\hbar G_1(&\hat{a}^+_{H_{+l},+\Omega}\hat{b}^+_{V_{-l},-\Omega} + \hat{a}^+_{H_{-l},+\Omega}\hat{b}^+_{V_{+l},-\Omega} \\ &+ \hat{a}^+_{V_{-l},+\Omega}\hat{b}^+_{H_{+l},-\Omega} + \hat{a}^+_{V_{+l},+\Omega}\hat{b}^+_{H_{-l},-\Omega}) + H.C., \end{aligned} \tag{2}$$

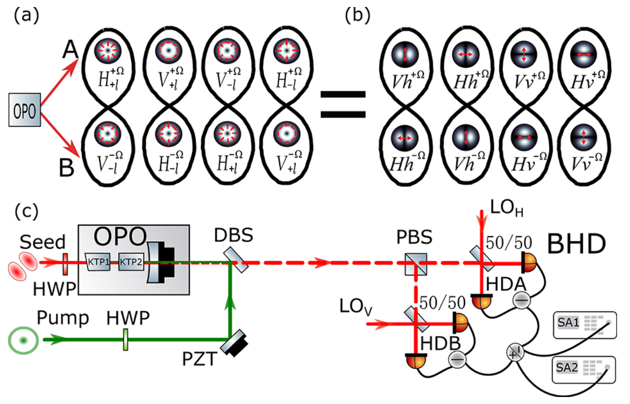

Fig. 2. Experimental schematic of the spin–orbit modes entanglement generation and measurement. (a) OPO outputs four pairs of spin–orbit modes entanglement in the first-order frequency sideband. (b) Measurements of spin–orbit modes entanglement are equivalent to verify the HG entanglement. (c) Experimental layout. KTP1 and KTP2, nonlinear crystals; DBS, dichroic beam splitter; HWP, half-wave plate; PZT, piezoelectric transducer; PBS, polarization beam splitter; BHD, balanced homodyne detection; LO, local oscillator; SA, spectrum analyzer.

where $\hat{a}^+$ and $\hat{b}^+$ are photon creation operators of downconverted photons A and B, and the parameter G_1 regulates the interaction strength. It explicitly shows a spin–orbit modes entanglement of the system, see Fig. 2(a). Since the VV modes are composed of a set of orthogonal HG modes ($\hat{a}_{H_{\pm l}} = (\hat{a}_{Hh} \pm \hat{a}_{Vv})/\sqrt{2}$, $\hat{a}_{V_{\mp l}} = (\hat{a}_{Vh} \pm \hat{a}_{Hv})/\sqrt{2}$), we can measure the spin–orbit modes entangled light field by the complete entanglement measurement of the first-order HG mode, as illustrated in Fig. 2(b), where Hh, Hv, Vh, and Vv denote the Hermite–Gaussian (HG) modes $h(HG_{10})$ and $v(HG_{01})$ for horizontal (H) and vertical (V) polarization, respectively.

The experimental setup is shown in Fig. 2(c). The multimode OPO is driven by the LG pump mode to generate spin–orbit modes entanglement and is then detected by balanced homodyne detection (BHD) with the spatial and frequency tailed local field. The cavity consists of two crystals ($3 \times 3 \times 5$ mm) and a mirror. The potassium titanyl phosphate (KTP1) with wedge angle of 1 degree is used for nonlinear interaction, and the middle crystal KTP2 is used for dispersion and astigmatism compensation. We conduct experiments under an optimal entanglement condition, by controlling the KTP temperature independently and locking the OPO with a 45° linear polarization $HG_{10}^{45^\circ}$ seed beam, see more details in Supplement 1.

To prove the existence of quadrature entanglement between two VV modes, we measure the quadrature quantum noise of

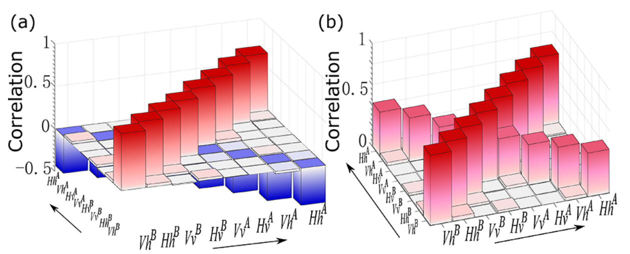

Fig. 3. Covariance matrix of the HG modes via measurements of the (a) amplitude and (b) phase quadrature quantum noise.

the first-order HG modes. By performing a simple basis transformation from the VV modes to HG modes, it is easy to show that $\hat{X}_{H_{\pm l}} = (\hat{X}_{Hh} \pm \hat{X}_{Vv})/\sqrt{2}$, $\hat{X}_{V_{\mp l}} = (\hat{X}_{Vh} \pm \hat{X}_{Hv})/\sqrt{2}$, $\hat{Y}_{H_{\pm l}} = (\hat{Y}_{Hh} \pm \hat{Y}_{Vv})/\sqrt{2}$ and $\hat{Y}_{V_{\mp l}} = (\hat{Y}_{Vh} \pm \hat{Y}_{Hv})/\sqrt{2}$, where $\hat{X}$ and $\hat{Y}$ are the amplitude and phase quadratures of the modes denoted by the lower indices. According to the criterion [24,25], CV spin–orbit modes entanglement can be witnessed if

$$\begin{aligned}
&\Delta^2(\hat{X}^A_{H^{+\Omega}_{+l}} + \hat{X}^B_{V^{-\Omega}_{-l}}) + \Delta^2(\hat{Y}^A_{H^{+\Omega}_{+l}} - \hat{Y}^B_{V^{-\Omega}_{-l}}) = \frac{1}{2}(\Delta^2(\hat{X}^A_{Hh} + \hat{X}^B_{Vh}) \\
&\quad + \Delta^2(\hat{X}^A_{Vv} + \hat{X}^B_{Hv}) + \Delta^2(\hat{Y}^A_{Hh} - \hat{Y}^B_{Vh}) + \Delta^2(\hat{Y}^A_{Vv} - \hat{Y}^B_{Hv}))<2, \\
&\Delta^2(\hat{X}^A_{H^{+\Omega}_{-l}} + \hat{X}^B_{V^{-\Omega}_{+l}}) + \Delta^2(\hat{Y}^A_{H^{+\Omega}_{-l}} - \hat{Y}^B_{V^{-\Omega}_{+l}}) = \frac{1}{2}(\Delta^2(\hat{X}^A_{Hh} + \hat{X}^B_{Vh}) \\
&\quad + \Delta^2(\hat{X}^A_{Vv} + \hat{X}^B_{Hv}) + \Delta^2(\hat{Y}^A_{Hh} - \hat{Y}^B_{Vh}) + \Delta^2(\hat{Y}^A_{Vv} - \hat{Y}^B_{Hv}))<2, \\
&\Delta^2(\hat{X}^A_{V^{+\Omega}_{-l}} + \hat{X}^B_{H^{-\Omega}_{+l}}) + \Delta^2(\hat{Y}^A_{V^{+\Omega}_{-l}} - \hat{Y}^B_{H^{-\Omega}_{+l}}) = \frac{1}{2}(\Delta^2(\hat{X}^A_{Vh} + \hat{X}^B_{Hh}) \\
&\quad + \Delta^2(\hat{X}^A_{Hv} + \hat{X}^B_{Vv}) + \Delta^2(\hat{Y}^A_{Vh} - \hat{Y}^B_{Hh}) + \Delta^2(\hat{Y}^A_{Hv} - \hat{Y}^B_{Vv}))<2, \\
&\Delta^2(\hat{X}^A_{V^{+\Omega}_{+l}} + \hat{X}^B_{H^{-\Omega}_{-l}}) + \Delta^2(\hat{Y}^A_{V^{+\Omega}_{+l}} - \hat{Y}^B_{H^{-\Omega}_{-l}}) = \frac{1}{2}(\Delta^2(\hat{X}^A_{Vh} + \hat{X}^B_{Hh}) \\
&\quad + \Delta^2(\hat{X}^A_{Hv} + \hat{X}^B_{Vv}) + \Delta^2(\hat{Y}^A_{Vh} - \hat{Y}^B_{Hh}) + \Delta^2(\hat{Y}^A_{Hv} - \hat{Y}^B_{Vv}))<2.
\end{aligned} \tag{3}$$

Using the transformation, the criterion reduces to verification between HG modes. Thus, by measuring the amplitude and phase quadrature variances of HG modes, entanglement between the VV modes can be witnessed.

The quadrature variances of the HG modes are analyzed using BHD with a spatially and frequency tailored local oscillator (LO) mode. We measure 48 correlation variances in the amplitude quadrature and phase quadrature with measurement basis $((\hat{a}_{Hh^{\pm\Omega}}, \hat{a}_{Vv^{\mp\Omega}})$, $(\hat{a}_{Hv^{\pm\Omega}}, \hat{a}_{Vh^{\mp\Omega}})$, $(\hat{a}_{Hh^{\pm\Omega}}, \hat{a}_{Vh^{\mp\Omega}})$, $(\hat{a}_{Hv^{\pm\Omega}}, \hat{a}_{Vv^{\mp\Omega}})$, $(\hat{a}_{Hh^{\pm\Omega}}, \hat{a}_{vac})$, $(\hat{a}_{Vv^{\pm\Omega}}, \hat{a}_{vac})$, $(\hat{a}_{Vh^{\pm\Omega}}, \hat{a}_{vac})$, $(\hat{a}_{Hv^{\pm\Omega}}, \hat{a}_{vac}))$, see the power spectrum density data and details in Supplement 1. Then, we have the covariance matrix of HG basis (see Fig. 3), where the covariance matrix elements are defined as $Cov(\hat{x}_i, \hat{x}_j) = \langle \hat{x}_i\hat{x}_j + \hat{x}_j\hat{x}_i \rangle /2 - \langle \hat{x}_i \rangle \langle \hat{x}_j \rangle$, subscript $i, j = Vh^{\pm\Omega}, Hh^{\pm\Omega}, Vv^{\pm\Omega}, Hv^{\pm\Omega}$ refer to HG modes with horizontal (vertical) polarization at positive (negative) frequency sideband and $x = X, Y$ to amplitude and phase quadrature. The correlation between the two HG modes is shown on the anti-symmetric axis, and excess noise occurs on the symmetric axis. It should be noted that the blue peaks (negative value) denote anti-correlation.

According to the measurement results and Eq. (3), we have proven that the OPO produces quadrature entanglement between these VV modes. Furthermore, the entanglement can be generalized to an arbitrary first-order VV mode. By performing unitary transformations ($Hh \rightleftharpoons Vh$ and $Hv \rightleftharpoons Vv$) on beam "B" with a half-wave plate, it changes the VV modes ($V_{-l} \rightleftharpoons H_{+l}$ and $V_{+l} \rightleftharpoons H_{-l}$), and Eq. (4) is the result:

$$\begin{aligned}
&\Delta^2(\hat{X}^A_{H^{+\Omega}_{+l}} + \hat{X}^B_{H^{-\Omega}_{+l}}) + \Delta^2(\hat{Y}^A_{H^{+\Omega}_{+l}} - \hat{Y}^B_{H^{-\Omega}_{+l}}) = 1.04 \pm 0.02<2, \\
&\Delta^2(\hat{X}^A_{H^{+\Omega}_{-l}} + \hat{X}^B_{H^{-\Omega}_{-l}}) + \Delta^2(\hat{Y}^A_{H^{+\Omega}_{-l}} - \hat{Y}^B_{H^{-\Omega}_{-l}}) = 0.99 \pm 0.02<2, \\
&\Delta^2(\hat{X}^A_{V^{+\Omega}_{-l}} + \hat{X}^B_{V^{-\Omega}_{-l}}) + \Delta^2(\hat{Y}^A_{V^{+\Omega}_{-l}} - \hat{Y}^B_{V^{-\Omega}_{-l}}) = 1.15 \pm 0.02<2, \\
&\Delta^2(\hat{X}^A_{V^{+\Omega}_{+l}} + \hat{X}^B_{V^{-\Omega}_{+l}}) + \Delta^2(\hat{Y}^A_{V^{-\Omega}_{+l}} - \hat{Y}^B_{V^{-\Omega}_{+l}}) = 1.13 \pm 0.02<2.
\end{aligned} \tag{4}$$

The arbitrary VV mode is expressed with the four orthogonal VV modes, $\hat{a}_{Arb} = k_1\hat{a}_{H_{+l}} + k_2\hat{a}_{H_{-l}} + k_3\hat{a}_{V_{-l}} + k_4\hat{a}_{V_{+l}}$, $\sum_{i=1}^{4} k_i^2 = 1$. Hence, the inseparability of arbitrary VV modes in beams A and B is

$$\begin{aligned}
&\Delta^2(\hat{X}^A_{Arb} + \hat{X}^B_{Arb}) + \Delta^2(\hat{Y}^A_{Arb} - \hat{Y}^B_{Arb}) \\
&= 1.04k_1^2 + 0.99k_2^2 + 1.15k_3^2 + 1.13k_4^2<2.
\end{aligned} \tag{5}$$

It shows CV entanglement between two arbitrary VV modes on HOPS. The potential application is to realize the blind state transfer of the quantum state on a HOPS, especially the determination teleportation of a high-dimensional single photon by combining the CV high-dimensional entanglement and discrete-variable technique, for example, the deterministic quantum teleportation of a single photon with multiple degrees [26,27].

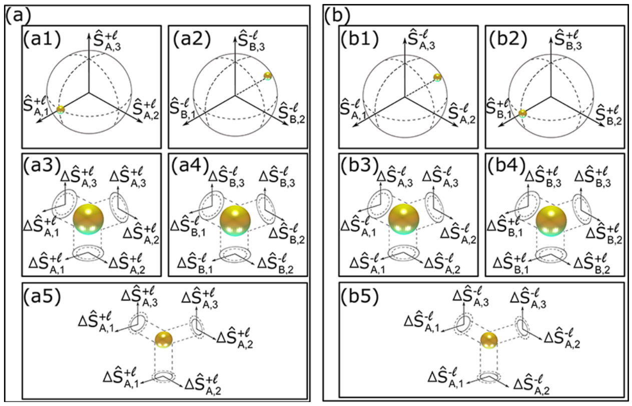

Fig. 4. Entanglement descriptions mapped on higher-order Poincaré sphere. (a1),(a2) Output beam A locates on $\hat{S}_1^{+l}$ while beam B on $\hat{S}_1^{-l}$. (a3) Noise volume of beam A before any measurement of beam B, and (a4) vice versa. (a5) Conditional knowledge of beam A given measurements of $\hat{S}_1^{-l}$ and $\hat{S}_2^{-l}$ and $\hat{S}_3^{-l}$ on beam B. (b1),(b2) Output beam A locates on $\hat{S}_1^{-l}$ while beam B on $\hat{S}_1^{+l}$. (b3),(b4) Noise volume of beams A and B when measuring them individually. (b5) Conditional knowledge of beam A given measurements of $\hat{S}_1^{+l}$ and $\hat{S}_2^{+l}$ and $\hat{S}_3^{+l}$ on beam B. The dashed circles show the SNL. If the conditional knowledge is better than the SNL, the modes are entangled.

We now proceed by characterizing the variances of the Stokes parameters that define the position of the state on the HOPS. The beams H_{+l} and V_{+l} reside in the $\hat{S}_1^{+l}$ region [Figs. 4(a1) and 4(a2)], whereas the beams V_{-l} and H_{-l} reside in the $\hat{S}_1^{-l}$ region [Figs. 4(b1) and 4(b2)]. Since we take 45° linear polarization $HG_{10}^{45^\circ}$ as the seed beam, $\alpha_{H_{+l}} = \alpha_{V_{-l}} = \sqrt{2}\alpha$ and $\alpha_{H_{-l}} = \alpha_{V_{+l}} = 0$. The fluctuations of HOPS Stokes operators of the two output beams (A,B) are then given by

$$\begin{aligned}
\Delta\hat{S}_{j,1}^{+l} &= \alpha_{j,H_{+l}}\Delta X_{j,H_{+l}} = \alpha\Delta X^j_{Hh} + \alpha\Delta X^j_{Vv}, \\
\Delta\hat{S}_{j,2}^{+l} &= \alpha_{j,H_{+l}}\Delta X_{j,V_{+l}} = \alpha\Delta X^j_{Vh} - \alpha\Delta X^j_{Hv}, \\
\Delta\hat{S}_{j,3}^{+l} &= \alpha_{j,H_{+l}}\Delta Y_{j,V_{+l}} = \alpha\Delta Y^j_{Vh} - \alpha\Delta Y^j_{Hv} \quad (j = A, B),
\end{aligned} \tag{6}$$

$$\begin{aligned}
\Delta\hat{S}_{j,1}^{-l} &= -\alpha_{j,V_{-l}}\Delta X_{j,V_{-l}} = -\alpha\Delta X^j_{Vh} - \alpha\Delta X^j_{Hv}, \\
\Delta\hat{S}_{j,2}^{-l} &= \alpha_{j,V_{-l}}\Delta X_{j,H_{-l}} = \alpha\Delta X^j_{Hh} - \alpha\Delta X^j_{Vv}, \\
\Delta\hat{S}_{j,3}^{-l} &= \alpha_{j,V_{-l}}\Delta Y_{j,H_{-l}} = \alpha\Delta Y^j_{Hh} - \alpha\Delta Y^j_{Vv} \quad (j = B, A).
\end{aligned} \tag{7}$$

According to the definition of correlation variance, $V_\pm(\hat{S}_{A,k}^{+l}, \hat{S}_{B,k}^{-l}) = \Delta^2(\hat{S}_{A,k}^{+l} \pm \hat{S}_{B,k}^{-l})/\Delta^2((\hat{S}_{A,k}^{+l})^{coh} + (\hat{S}_{B,k}^{-l})^{coh})$, there is quantum correlation between the uncertainties of the Stokes operators if $V_\pm<1$. In our experiment, there are two output cases. When output beam A locates on sphere $\hat{S}_1^{+l}$ while beam B on $\hat{S}_1^{-l}$ [Fig. 4(a)], we infer that the noise variances of beam A before any measurement of beam B are $V(\hat{S}^{+l}_{A,1}) = 1.36 \pm 0.01$, $V(\hat{S}^{+l}_{A,2}) = 1.36 \pm 0.01$, and $V(\hat{S}^{+l}_{A,3}) = 1.40 \pm 0.01$ [Fig. 4(a3)]. The noise levels of all the three Stokes variables are above the shot noise limit (SNL), and vice versa [Fig. 4(a4)], $V(\hat{S}^{-l}_{B,1}) = 1.33 \pm 0.01$, $V(\hat{S}^{-l}_{B,2}) = 1.36 \pm 0.01$, $V(\hat{S}^{-l}_{B,3}) = 1.36 \pm 0.01$. Implementing joint measurements of A and B, we have $V_{-}(\hat{S}^{+l}_{A,1}, \hat{S}^{-l}_{B,1}) = 0.55 \pm 0.01 < 1$, $V_{+}(\hat{S}^{+l}_{A,2}, \hat{S}^{-l}_{B,2}) = 0.54 \pm 0.01 < 1$, and $V_{-}(\hat{S}^{+l}_{A,3}, \hat{S}^{-l}_{B,3}) = 0.54 \pm 0.01 < 1$. In other words, after the measurement of beam B, the conditional noise volume of beam A becomes a small ball shape on HOPS [Fig. 4(a5)]. When output beam A locates on sphere $\hat{S}^{-l}_{1}$ while beam B on $\hat{S}^{+l}_{1}$ [Fig. 4(b)], the noise variances of beam A before any measurement of beam B are $V(\hat{S}^{-l}_{A,1}) = 1.36 \pm 0.01$, $V(\hat{S}^{-l}_{A,2}) = 1.40 \pm 0.01$, $V(\hat{S}^{-l}_{A,3}) = 1.40 \pm 0.01$ (Fig. 4(b3)), and $V(\hat{S}^{+l}_{B,1}) = 1.34 \pm 0.01$, $V(\hat{S}^{+l}_{B,2}) = 1.36 \pm 0.01$, $V(\hat{S}^{+l}_{B,3}) = 1.36 \pm 0.01$ [Fig. 4(b4)] for the beam B without any measurement of beam A. Likewise, the relevant variances are $V_{-}(\hat{S}^{-l}_{A,1}, \hat{S}^{+l}_{B,1}) = 0.54 \pm 0.01 < 1$, $V_{+}(\hat{S}^{-l}_{A,2}, \hat{S}^{+l}_{B,2}) = 0.55 \pm 0.01 < 1$, and $V_{-}(\hat{S}^{-l}_{A,3}, \hat{S}^{+l}_{B,3}) = 0.54 \pm 0.01 < 1$. It clearly shows the spin–orbit total angular momentum Stokes entanglement associated with Stokes operators $\hat{S}^{+l}_{3}$ and $\hat{S}^{-l}_{3}$, where the $\hat{S}^{\pm l}_{3}$ refers to the total angular momentum including SAM and OAM. In addition, unlike the cigar-shaped uncertainty volume of SAM or OAM entanglement, the three-dimensional operators ($\hat{S}^{\pm l}_{1}$, $\hat{S}^{\pm l}_{2}$, and $\hat{S}^{\pm l}_{3}$) can be simultaneously below the SNL [Figs. 4(a5) and 4(b5)]. This type of entanglement is more useful for simultaneous measurements in three dimensions and loading of more information.

In conclusion, we experimentally generate CV spin–orbit modes entanglement with a type-II OPO and characterize the HOPS Stokes parameters entanglement. The spin–orbit total angular momentum Stokes entanglement is demonstrated. By performing a unitary transformations on one beam of the entangled pair, arbitrary spin–orbit modes entanglement on HOPS can be realized. Benefiting from its classic characteristics, the spin–orbit modes can be used to study the angular momentum transfer between two DoFs [28] and practical optical manipulations [29]. In addition, the spin–orbit modes entanglement cannot only be used for quantum communication based on free space and optical fibers, it can also be used for Bell-inequality tests from continuous variable and to realize super-resolution imaging in stimulated emission depletion (STED) microscopy beyond the quantum limit [30] based on VV mode squeezing. In addition, it is promising to generate novel kinds of cluster states for quantum computation protocols. The hidden potential of CV spin–orbit modes entanglement remains to be explored.

Funding. National Natural Science Foundation of China (12074233); National Key Research and Development Program of China (2016YFA0301404, 2021YFC2201802); Shanxi Scholarship Council of China (2021-05); Natural Science Foundation of Shanxi Province (1331).

Disclosures. The authors declare no conflicts of interest.

Data availability. Data underlying the results presented in this paper are not publicly available at this time but may be obtained from the authors upon reasonable request.

Supplemental document. See Supplement 1 for supporting content.

REFERENCES

1. K. Bliokh, F. Rodríguez-Fortuno, F. Nori, and A. Zayats, Nat. Photonics **9**, 796 (2015).
2. A. Forbes and I. Nape, AVS Quantum Sci. **1**, 011701 (2019).
3. K. Toyoda, F. Takahashi, S. Takizawa, Y. Tokizane, K. Miyamoto, R. Morita, and T. Omatsu, Phys. Rev. Lett. **110**, 143603 (2013).
4. S. Berg-Johansen, F. Töppel, B. Stiller, P. Banzer, M. Ornigotti, E. Giacobino, G. Leuchs, A. Aiello, and C. Marquardt, Optica **2**, 864 (2015).
5. E. Karimi, F. Cardano, M. Maffei, C. de Lisio, L. Marrucci, R. W. Boyd, and E. Santamato, Phys. Rev. A **89**, 032122 (2014).
6. J. T. Barreiro, T.-C. Wei, and P. G. Kwiat, Phys. Rev. Lett. **105**, 030407 (2010).
7. M. H. M. Passos, A. de Oliveira Jr., M. C. de Oliveira, A. Z. Khoury, and J. A. O. Huguenin, Phys. Rev. A **102**, 062601 (2020).
8. V. D'Ambrosio, E. Nagali, S. P. Walborn, L. Aolita, S. Slussarenko, L. Marrucci, and F. Sciarrino, Nat. Commun. **3**, 961 (2012).
9. J. Liu, S.-M. Li, L. Zhu, A.-D. Wang, S. Chen, C. Klitis, C. Du, Q. Mo, M. Sorel, S.-Y. Yu, X.-L. Cai, and J. Wang, Light: Sci. Appl. **7**, 17148 (2018).
10. D. Cozzolino, E. Polino, M. Valeri, G. Carvacho, D. Bacco, N. Spagnolo, L. K. K. Oxenløwe, and F. Sciarrino, Adv. Photonics **1**, 046005 (2019).
11. P. Grangier, R. E. Slusher, B. Yurke, and A. LaPorta, Phys. Rev. Lett. **59**, 2153 (1987).
12. W. P. Bowen, R. Schnabel, H. A. Bachor, and P. K. Lam, Phys. Rev. Lett. **88**, 093601 (2002).
13. N. Korolkova, G. Leuchs, R. Loudon, T. C. Ralph, and C. Silberhorn, Phys. Rev. A **65**, 052306 (2002).
14. M. T. L. Hsu, W. P. Bowen, and P. K. Lam, Phys. Rev. A **79**, 043825 (2021).
15. M. Lassen, G. Leuchs, and U. L. Andersen, Phys. Rev. Lett. **102**, 163602 (2009).
16. C. Cai, L. Ma, J. Li, H. Guo, K. Liu, H. Sun, and J. Gao, Opt. Express **26**, 5724 (2018).
17. K. Liu, J. Guo, C. Cai, S. Guo, and J. Gao, Phys. Rev. Lett. **113**, 170501 (2014).
18. R. B. Rodrigues, G. B. Alves, R. F. Barros, C. E. R. Souza, and A. Z. Khoury, Phys. Rev. A **105**, 013510 (2022).
19. C. Gabriel, A. Aiello, W. Zhong, T. G. Euser, N. Y. Joly, P. Banzer, M. Fortsch, D. Elser, U. L. Andersen, C. Marquardt, P. S. Russell, and G. Leuchs, Phys. Rev. Lett **106**, 060502 (2011).
20. V. Chille, S. Berg-Johansen, M. Semmler, P. Banzer, A. Aiello, G. Leuchs, and C. Marquardt, Opt. Express **24**, 12385 (2016).
21. R. F. Barros, G. B. Alves, and A. Z. Khoury, Phys. Rev. A **103**, 023511 (2021).
22. G. Milione, H. I. Sztul, D. A. Nolan, and R. R. Alfano, Phys. Rev. Lett. **107**, 053601 (2011).
23. K. Liu, C. X. Cai, J. Li, L. Ma, H. X. Sun, and J. R. Gao, Appl. Phys. Lett. **113**, 261103 (2018).
24. L.-M. Duan, G. Giedke, J. I. Cirac, and P. Zoller, Phys. Rev. Lett. **84**, 2722 (2000).
25. R. Simon, Phys. Rev. Lett. **84**, 2726 (2000).
26. X. L. Wang, X. D. Cai, Z. E. Su, M. C. Chen, D. Wu, L. Li, N. L. Liu, C. Y. Lu, and J. W. Pan, Nature **518**, 516 (2015).
27. S. Takeda, T. Mizuta, M. Fuwa, P. van Loock, and A. Furusawa, Nature **500**, 315 (2013).
28. B. Pinheiro da Silva, W. T. Buono, L. J. Pereira, D. S. Tasca, K. Dechoum, and A. Z. Khoury, Nanophotonics **11**, 771 (2022).
29. P. Shi, L. Du, and X. Yuan, Opt. Express **26**, 23449 (2018).
30. N. P. Mauranyapin, A. Terrason, and W. P. Bowen, "Quantum Biotechnology," arxiv, arXiv:2111.02021 (2021).